Towards a microwave imaging device for cerebrovascular diseases monitoring: from numerical modeling to experimental testing

Terms of use:

(Article begins on next page)

14 January 2025

Towards a Microwave Imaging Device for Cerebrovascular Diseases Monitoring: from Numerical Modeling to Experimental Testing

David O. Rodriguez-Duarte, Jorge A. Tobón Vasquez, Cristina Origlia, Rosa Scapaticci, Giovanna Turvani, Mario R. Casu, Lorenzo Crocco and Francesca Vipiana

Abstract   This chapter presents the design, realization, and validation of a full-fledged device for imaging-based detection and monitoring of cerebrovascular diseases via microwave technology. The designed system is a compact and low-complexity prototype with a wearable twenty-two-element antenna array able to perform continuous real-time follow-up of a brain stroke evolution. The imaging algorithm exploits a differential scheme that receives the scattering matrices collected at two different instants and reconstructs tridimensional images relying on the distorted Born approximation. Furthermore, it employs the singular value decomposition of the discretized scattering operator computed via full-wave simulations via high-realistic models and an EM solver based on an in-house finite element method. The system is numerically and experimentally tested on post-onset scenarios, showing the capability to localize and monitor the progression of hemorrhage and ischemia zones with centimetric spatial resolution. Moreover, it details the manufacturing of the custom radiating elements and the human-like head and non-static stroke testing phantoms used during the experimental testing.

Key words: Biomedical electromagnetic imaging, microwave imaging, brain stroke monitoring, distorted Born approximation, flexible antennas, hemorrhagic stroke, ischemic stroke, inverse scattering, microwave antenna array, propagation.

D. O. Rodriguez-Duarte · F. Vipiana
Politecnico di Torino, Turin, Italy
e-mail: david.rodriguez@polito.it

F. Vipiana
e-mail: francesca.vipiana@polito.it

J. A. Tobón Vasquez · C. Origlia · G. Turvani · M. R. Casu
Politecnico di Torino, Turin, Italy

R. Scapaticci · L. Crocco
IREA-CNR, Institute for Electromagnetic Sensing of the Environment, National Research
Council of Italy, Naples, Italy

1 Introduction

Cerebrovascular diseases are disorders in which an area of the brain is temporarily or permanently affected by ischemia or bleeding, involving one or more cerebral blood vessels in the pathological process. The flow alterations may occur from the stenosis (vessel narrowing), thrombosis (clot formation), or embolism (blockage) that provokes a lack of sufficient blood flow, affecting brain tissue and causing an ischemic (IS) stroke. This latter is the most frequent stroke category, counting for 85 % of all cases [1]. Commonly, during the IS stroke, the arteries are not entirely obstructed, and a meager bloodstream trickles to the brain, leading to the appearance of two distinct areas, the core, and the penumbra. The blood is almost completely cut off in the core, starving the cells within minutes. The penumbra is a much more extensive area surrounding the dead cells in the core, consisting of injured and malfunctioning cells (idling cells), which can remain in this state for about three hours before they die. Depending on the time window, physicians treat the IS stroke by removing the blocking and restoring blood flow to the brain using thrombolytic drugs or mechanical devices. However, the medication increases the risk of intracranial hemorrhage. The remaining 15 % of cases are hemorrhagic strokes, which are the most deadly. Here, blood vessel rupture or leaks within the artery or on its surface may cause bleeding and damage to the brain. If the vessel breaks inside the brain tissue, it is an intracerebral hemorrhage (ICH), while if it breaks on the brain surface, it is termed subarachnoid hemorrhage. It is usually surgically treated to relieve intracranial pressure caused by bleeding.

Regardless of the stroke typology, a prompt diagnosis is crucial for effective treatment, i.e., an early detection, localization, and classification of the disorder, and subsequent medical care that restore blood flow as soon as possible, mitigating collateral effects. Once the stroke onset and its first symptoms appear, the protocol suggests calling for an ambulance or approaching a medical center/hospital immediately. The medical personnel stabilizes the patient and preliminary assesses his condition. The next 8-hour stage is crucial: clinicians and therapists monitor and evaluate the patient, supporting their prognosis and intervention with imaging-based technologies such as magnetic resonance imaging (MRI) and computerized X-ray tomography (CT). Finally, the patient is hospitalized and monitored due to the high risk of another stroke.

MRI and CT are the current gold standard for medical imaging support, both well-established technologies that deliver highly reliable diagnostic information. However, they have intrinsic drawbacks in terms of portability, cost, time-consume, and safeness (for CT only) that limit their applicability [2, 3]. For instance, an MRI or a CT scanner is bulky and cannot be normally installed in an ambulance or mobile care unit. Moreover, the examination time, the availability of the devices, the costs, and the ionizing radiations (in the CT case), do not allow these technologies to perform real-time monitoring in the emergency department or later at the patient's bedside. In this context, microwave imaging (MWI) has emerged as an attractive non-ionizing, low-intensity, and cost-effective complementary approach, enabling pre-

hospital diagnosis of the stroke, bedside brain imaging, and continuous monitoring during the post-acute stage, albeit at the cost of a lower resolution [4–16].

MWI relies on the contrast of the electrical properties (permittivity and conductivity) exhibited by the healthy brain tissues and the stroke-affected ones at microwave frequencies to identify their typology and physio-pathological status. For instance, the electrical properties of the affected area decrease during an IS stroke due to the reduction of the blow flow and, conversely, increase in the case of bleeding. This technique illuminates the body with low-power EM waves in the GHz range of the spectrum, then uses the resultant back-scattered signals to generate images of the internal structures. Hence, MWI devices exploit the non-invasive and harmless nature of microwaves together with the current high-performance microwave hardware and computing power to complement and overcome the limitation of cost, portability, and harmfulness of traditional diagnostic techniques. Summing up, MWI technology:

- exhibits favorable penetration depths that allow imaging of deeper tissues in the human body as compared to other emerging modalities (e.g., optical techniques);
- is entirely harmless since the involved waves are non-ionizing and used in very low doses (low-power EM waves);
- is convenient for the healthcare system, providing mobile and low-cost imaging platforms, backup for advancement in the mobile industry and microwave devices in recent years.

A typical MWI device is made by an array of antennas, which is in charge of probing the region on the body under examination and collect the back-scattered waves data. Moreover, the device must be equipped with a suitable data processing algorithm in charge of pursuing the solution of the non-linear inverse scattering problem to be faced in order to retrieve the EM properties of inspected tissue from the data. In the specific application of brain stroke, several academic [4–12], and industrial prototypes [13–16] have been developed. For example, [4,5] show a 16-antenna-array-ring system, where the matching medium consists of heat-sealed polyethylene bags filled with a water-glycerine-based liquid, and a two-dimensional (2-D) tomographic approach to resolve the non-linear inversion in Lebesgue spaces. [6,7] present a device with an 8-antenna array submerged in glycerin as a matching medium, performing a 2-D non-linear microwave tomography imaging via a distorted Born iterative method (DBIM) with GPU-accelerated Finite-difference time-domain (FDTD). [8] introduces a novel hybrid imaging system using both a radar approach and a frequency approach, testing it with an 8-element array of ultra-wideband Bowtie antenna in a 2-D configuration. [9] poses a 14-antenna-array system, working with a novel polar sensitivity encoding (PSE) algorithm to locate the stroke. Besides, in [10], they propose a flexible-24-antenna cap and three-dimensional (3-D) tomography imaging technique, achieving the location of the stroke in complex scenarios, yet with limited shape retrieval and non-monitoring testing. Moreover, in [11], the authors of this chapter developed a 24-antennas system employing a solid graphite-rubber mixture as a matching medium, and approaching the detection and localization stroke targets via a 3-D imaging algorithm. Additionally, they optimize the system, reducing its dimensions and number of antennas, as well as perform real-time imaging-based

monitoring of hemorrhages and ischemie in mimicked lab scenarios [12], which further assessed in this chapter.

On the other hand, the Strokefinder, the EMTensor BrainScanner, and the EMVision Scanner are devices developed by companies. Medfield Diagnostics developed the Strokefinder, a low-complexity and patient-adaptable device made of 8 antennas, aiming to discriminate the stroke typology early in the pre-hospital stage [13, 14]. This first device does not aim to generate images of the stroke. However, it is an excellent example of narrowing the clinical problem and the system functionalities that still retrieves a piece of vital information for doctors and physicians. The second device, EMTensor BrainScanner [15], performs tomographic imaging and approaches in-ambulance and bedside scenarios. However, it uses a highly complex system consisting of 177 loaded and truncated waveguides (radiating elements) in its initial version, increasing the complexity of data processing inherently. The last example, EMVision Scanner [16], is also a tomographic device with encouraging results in the undergoing clinical trials.

This chapter presents the develops and testing of the prototype device presented in [11, 12]. In the following, we present the mathematical background behind the image formation and the new system design, which is synthetically tested using different virtual scenarios, providing a preview of the system's capabilities. Second, the whole system is assessed using non-static mimicked clinical scenarios. This part covers the experimental setup, including the manufacturing and characterization of the different elements used during the experimental testing. Finally, all numerical and experimental results are gathered, closing up with the conclusions and perspectives.

2 Microwave-based Stroke Monitoring

2.1 Imaging algorithm

This section first discusses the principles and mechanisms associated with MWI monitoring. Then, it describes the algorithm used to deal with the intrinsic nonlinearity and ill-posedness of the inverse scattering problem under the imaging-based follow-up task.

In this context, the direct problem involves calculating the scattered electric fields due to the evolution of the pathology when the monitoring device is illuminating the domain of interest (DOI). In other words, the temporal variation of the dielectric properties of the brain tissues in the stroke-affected area causes a change in the scattered field, stating a cause-and-effect relationship. In the inverse problem, the goal is to retrieve the EM properties from the scattered fields. This problem is ill-possed, due to the intrinsic loss of information arising from the fact the sought unknown is not directly probed but assessed through its footprint in the measured scattered field. To deal with the ill-posedness, the problem needs to be regularized, adding prior information related to the problem's physics [17]. Hence, regularization relies on limiting the family of possible solutions so that the family functions converge

to the exact solution, in the case of noise-free data, or to an optimal approximation, in the case of noisy data. In other words, regularization acts with the premise of intentionally using additional information to generate families of approximate solutions consistent with the given image.

Getting into the intended application, the input data are the S-parameters of an array of transceivers placed around the DOI. These parameters sample and describe the illuminating system in terms of the incoming and outgoing port waves, named a_p and b_q, given at the p-th and q-th antenna ports, respectively. Hence, the forward problem can be stated analytically as:

$$\Delta S(\mathbf{r}_p, \mathbf{r}_q; t_0, t_1) = -\frac{j\,\omega\,\varepsilon_b}{2\,a_p\,a_q} \int_{\text{DOI}} \mathbf{E}_p(\mathbf{r}, t_0) \cdot \mathbf{E}_q(\mathbf{r}, t_1) \, \Delta\chi(\mathbf{r}, t_0, t_1) \, d\mathbf{r}, \quad (1)$$

which indicates the scene variation with respect to a constitutive or shape object parameter and the field distribution [18]. In Eq. 1, ΔS is the differential scattering parameter, D is the volume of the domain of imaging, j is the imaginary unit, $\omega = 2\pi f$ is the angular frequency, ε is the complex permittivity distribution, b indicates a reference background scenario, and the symbol "$\cdot$" denotes the dot product. Furthermore, $\mathbf{E}_p(\mathbf{r}, t_0)$ and $\mathbf{E}_q(\mathbf{r}, t_1)$ are the nominal electric field vectors, i.e., the fields radiated by the p-th and q-th probe inside the DOI at the respective state, and

$$\Delta\chi(\mathbf{r}; t_0, t_1) = \frac{\varepsilon(\mathbf{r}, t_1) - \varepsilon(\mathbf{r}, t_0)}{\varepsilon_b(\mathbf{r})}, \quad (2)$$

is the spatial distribution of the normalized contrast, all referenced to the instants t_0 and t_1, respectively.

Notice that Eq. 1 presents a non-linear problem that iterative methods solve by posing it as an optimization task. Examples of these methods are the DBIM and the contrast source inversion (CSI) [19], [20], –Chap. "Assessment and Validation of 2-D and 3-D DBIM-TwIST Algorithm for Brain Stroke Detection and Differentiation." However, these methods require to solve the forward problem, that is, the heaviest computational part. Therefore they are not convenient for the targeted real-time application.

Another way to solve the nonlinear problem is to linearize it using the so-called Born approximation. It assumes mild overall perturbation of the electric field in the studied period, which is due to a "weak" and localized perturbation, as in the monitoring problem where the affection is concentrated in an area, and the examination times are user-controlled. Moreover, we approach the problem by applying the distorted version of the approximation considering the morphological variability of the patient. Therefore, the forward formulation is rewritten as:

$$\Delta S(\mathbf{r}_p, \mathbf{r}_q; t_0, t_1) = -\frac{j\,\omega\,\varepsilon_b}{2\,a_p\,a_q} \int_{\text{DOI}} \mathbf{E}_p^{ref}(\mathbf{r}) \cdot \mathbf{E}_q^{ref}(\mathbf{r}) \, \Delta\chi(\mathbf{r}, t_0, t_1) \, d\mathbf{r}, \quad (3)$$

where the field distributions at t_0 and t_1 are replaced by nominal reference one, $\mathbf{E}^{ref}$, consisting of a scenario representing the head as a single-tissue organ with the average complex permittivity of a brain. In a compact format, Eq. 3 is expressed as

$$\Delta S = \mathcal{L}\{\Delta \chi\}, \tag{4}$$

where $\mathcal{L}$ is the linear operator from the object space into the image space. The imaging operator kernel describes the system's response to a point source as a function of the observation position, forming the so-called point-spread function (PSF), which is an indicator of the resolution of the system.

To invert Eq. 4, first, the imaging kernel is built by applying a singular value decomposition (SVD) to the discretized integral operator and decomposing it in $\langle[u], [\sigma], [v]\rangle$, where σ_n, u_n and v_n are the n-th singular value, right and left singular vectors, respectively. Then, the differential contrast distribution is retrieved as:

$$\Delta \chi = \sum_{n=1}^{T} \frac{1}{\sigma_n} \langle \Delta S, u_n \rangle \, v_n, \tag{5}$$

where truncation index T acts as a regularizer parameter [17].

In summary, the imaging algorithm uses both an off-line part, compute-intensive but just done once, where the imaging kernel is generated and decomposed, and a real-time (fast) part facing the inversion. Figure 1 illustrates the general scheme of the imaging. Moreover, because the living tissues are linear media whose constitutive parameters do not depend on the field strength, we are dealing with a reciprocal network and ΔS is expected to be symmetric. Thus, in an N-port network, only $N(N+1)/2$ S-parameters are independent, representing the upper/lower triangular part of ΔS. Though, we do not employ the reflection self elements for the imaging, as further explained in Sec. 3, thus the number of independent parameters is reduced to $N(N-1)/2$, decreasing both the $\mathcal{L}$ and ΔS dimensions.
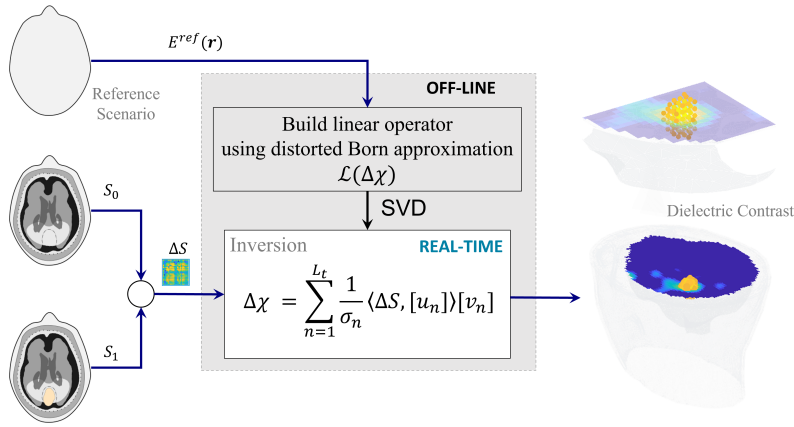

Fig. 1: Differential imaging algorithm scheme

2.2 Electromagnetic Modeling

To build the imaging kernel (operator), we computed $\mathbf{E}^{ref}$ from numerically modeled scenarios using realistic computer-aided design (CAD) models of the MWI prototype and the head, the nominal dielectric properties of all elements involved, and an electromagnetic (EM) finite element method (FEM) solver. In the specific, the properties of the head tissues are taken from [21] and hemorrhagic or ischemic ones from [22,23], while others are measured experimentally using the open-coaxial technique, as described in [24]. Besides, the geometrical models came from [25], and an in-house FEM implementation is exploited [26].

FEM is a numerical technique used to obtain an approximated solution to boundary-value problems described and governed by either differential or integrodifferential equations, such as Maxwell's equations [27]. It resolves the original problem approximating the solution with a finite number of subdomains in which simple interpolation functions change the unknown function with unknown coefficients. Then, the response is determined by solving the system of equations obtained by applying the Galerkin procedure. FEM is an optimum alternative to approach problems with complex architectures describing scenarios with arbitrary shapes and complex permittivity distributions, where interact, for example, biological tissues, as the head, with close-by radiating elements. In general, it follows the stages listed below:

- **Discretization of subdivision of the domain:** this is probably the most important part of FEM procedures because the way in which it is done directly affects the computer storage requirements, the computation time, and the accuracy of the results. In this work, we use tetrahedra, the simplest and best suited for arbitrary-volume domains, such as the tissues and organs within the head.
- **Selection of the interpolation functions:** provides an approximation of the unknown solution within the element. We use a first-order (linear) polynomial [27].
- **Formulation of the system of equations:** can be done using either the Ritz variational method [27] or the Galerkin one, which is used here.
- **Solution of the system of equations:** is the last step of the finite element analysis. In electromagnetics, it is usually associated with problems where exists a source or excitation, e.g., scattering problems.

In this work, the employed FEM uses edge-basis functions for the expansions, the curl-curl formulation for the electric field, and the Galerkin approach for testing [26, 28]. Also, regarding the boundary conditions, first, it applies the Dirichlet condition to the metallic surfaces, such as the radiating element of the antenna and the coaxial connectors, thus stating them as perfect electric conductors (PEC) surfaces. Secondly, it forces absorbing boundary conditions (ABC) on the contour surfaces of the cylindrical volume [28], simulation domain, that holds the whole system. The simulation volume is meshed using a tetrahedral base and subdivided using different density levels depending on the precision and importance of the discretized volume, e.g., finer on the port of the antennas. Moreover, the forcing elements of the system, essential components to retrieve the fields and compute the scattering parameters

accurately, are included via the antennas' coaxial feeding. Then, each antenna port is modeled as a section of a rigid coaxial cable with lossless Teflon, $\epsilon_r = 2.2$, as a substrate. To excite an antenna is enforced the tangential electric field, $\mathbf{E}^{\text{inc}}$, on the port surface, S_{port}, and proper boundary conditions are applied [26, 27]. The scattering parameter for each antenna pair, p and q, is then evaluated as

$$
S_{pq} = \begin{cases} \dfrac{\int_{S_{port}} \mathbf{E}_p \cdot \mathbf{E}_q^{\text{inc}*} \, dS}{\int_{S_{port}} |\mathbf{E}_q^{\text{inc}}|^2 \, dS} & \text{if } p \neq q \\ \dfrac{\int_{S_{port}} \mathbf{E}_q \cdot \mathbf{E}_q^{\text{inc}*} \, dS}{\int_{S_{port}} |\mathbf{E}_q^{\text{inc}}|^2 \, dS} - 1 & \text{if } p = q \end{cases}
\tag{6}
$$

where $\mathbf{E}_q^{\text{inc}}$ is the electric field forced in the excited port q and $\mathbf{E}_p$ is the electric field evaluated at the port p via the FEM solver. $\mathbf{E}_q^{\text{inc}}$ can be represented with the transverse electromagnetic (TEM) mode of the coaxial cable as

$$
\mathbf{E}_q^{\text{inc}} = \frac{V}{\sqrt{2\pi \ln (r_b/r_a)}} \frac{\hat{\rho}}{\rho},
\tag{7}
$$

where r_a and r_b are the internal and external radii of the coaxial cable, and ρ and $\hat{\rho}$ are the radial coordinate and radial unit vector from the center of the coaxial cable in the port plane [27]. The coefficient V is chosen to equal 1 V.

2.3 Design of a Low-complexity Microwave Imaging Device

As mentioned in the introduction, one of the benefits of employing MWI technology is to design portable devices with low cost and suitable imaging capabilities. With these features in mind, we describe the following design guidelines to design a low-complexity device, taking as reference the outcomes of [29, 30].

2.3.1 Operational Frequency and Matching Medium

Operational frequency and matching medium parameters are some of the most relevant to choose from while developing a MWI prototype for stroke follow-up. Their selection directly influences the incident power penetration and the spatial resolution. For instance, lower frequencies increase the penetration, but decrease the resolution, whereas the opposite occurs at high frequencies. Thus, these parameters are direct degrees of freedom for the device's design since the wave penetration depends on the electrical discontinuity, and the wavelength in the coupling medium dictates the resolution.

To select them, we follow the rigorous procedure proposed in [29] and numerically validated in [31], which guarantees low computation effort. It studies the propagating wave scenario of a multi-tissue head, considering the interaction between the head,

the coupling medium, and the electric incident field as a parallel transmission line network. Then, the simplified model assumes the head tissues (e.g., skin, fat, bone, cerebrospinal fluid (CSF), and average brain – grey and white matter –) and the matching medium as line segments, where the brain acts as a load. These segments are characterized by the estimated length of the actual radial thickness and the corresponding impedance, $Z_n = \sqrt{\mu_0/\varepsilon_0\varepsilon_t}$, where ε_t is the complex permittivity of each tissue. At the same time, ε_0 and μ_0 are the free space's permittivity and permeability. Meanwhile, the power source is considered into the matching medium in direct contact with the head.

Once modeled the scenario, the transmittance coefficient T is computed, describing the amount of power penetrating the head, defining it as [32]:

$$T = 1 - |\Gamma|^2, \tag{8}$$

where Γ is the reflection coefficient referenced to the interface plane entering the head. Then, there is a low-transmittance band between 1.5–2.5 GHz for any matching permittivity value from 1 to 80 [29]. Also, the operation in frequencies higher than 2.5 GHz may not be convenient due to 2 cm or less penetration depth, for tissues such as skin, bone, or CSF. Moreover, frequencies below 0.6 GHz reduce the spatial resolution too much, dictated by the background medium wavelength. Finally, the 0.6–1.5 GHz band is identified as an adequate operation frequency band while matching permittivity is higher than 10 and lower than 40, with minimum losses. So, from herein, we choose 1 GHz as the operating frequency. Regarding the matching medium, we decide to employ solid and flexible materials, with adjustable permittivity, which is set around 20.

2.3.2 Optimal Antenna Array Layout

The first intuitive idea while determining an optimal number of antennas is to use as many as possible since having more antennas means more information. However, the selection approach is not straightforward and should consider aspects such as the redundancy of the gathered information, physical constraints, and costs. Thus, we follow the methodology developed and tested in [30, 33], which is an instrument to find a good trade-off between stability and accuracy.

It consists of an SVD-based numerical analysis of the imaging kernel, considering the number of antennas, N_a, as a variable, and the operator condition number (CN), i.e., the ratio between the largest (first) and smallest (last) singular values, as studied parameter. CN indicates the robustness of the inversion to higher-level noise and modeling errors. Hence, the lower the CN, the more robust the inversion, but when N_a increases, whatever the antenna polarization, CN increases too. In fact, higher N_a means less distance between antenna elements, and the information gathered by close elements would be strongly dependent, or even redundant, while the measurement noise remains independent. This analysis is done in [30] for the head case, showing good compromise when $N_a \approx 24$. In this scenario, CN remains lower than the

dynamics and the SNR of a standard measurement system, which is about 90 dB. Moreover, the perforce does not improve considerably with double the antenna number, $N_a = 48$, getting CN≈100 dB, but it implies higher complexity and cost.

N_a and the antennas' distribution also directly affect the discretization error and the imaging accuracy. This error is a metric defined in [33], that considers the normalized difference between a case using a continuous (ideal) scanning surface ($N_a \approx \infty$) and a discretized case using a limited N_a. Moreover, it is worth noting that the system's dynamic also limits the imaging operator's accuracy. So, considering the monitoring application, the actual dynamic range available is around 30 dB, if we estimate the differential scattering as about 70 dB below and the dynamic range of a medium-performance VNA as 100 dB. Therefore, as [30] shows, working with about $20 - 30$ antennas is a good compromise also in terms of imaging accuracy.

Finally, we opt for a 22-antenna configuration placed on a head conformal array that, as shown later in the validation, demonstrates a centimetric resolution (around $\lambda/4$), agreeing with the findings in [30]. This selection also considers the head and antenna dimensions and keeps the low complexity, thus reducing cost.

3 Microwave Imaging Prototype and Experimental Setup

Considering the design guidelines, we detail the projected MWI system consisting of a 22-antenna array configuration, working with a vector network analyzer and a switching matrix, as shown in Fig. 2.
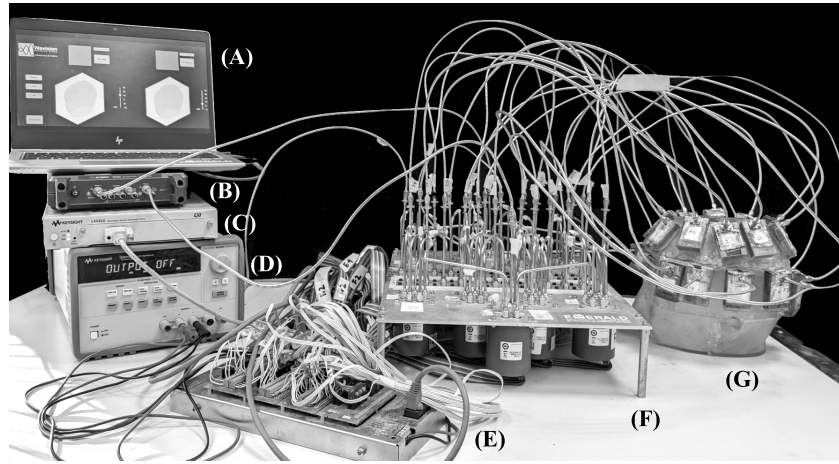
3.1 Antenna array

As aforementioned, we use a 22-antenna array configuration that is conformal to the head's upper part, reaching a good field coverage (see Sec. 4). Each antenna is positioned directly on the head surface, e.g., the skin in multi-tissue cases, and held by a fixed container in the experimental case.

The antenna element is an optimized back-fed monopole consisting of a triangular radiant part and a double-stub line, as shown in Fig. 3 (a). It is printed on flexible commercial 50 μm-thickness Polyimide film, placing the ground (GND) plane on the backside. Then, the printed segments are stacked in a two-layer structure, forming a joint antenna module with enough flexibility to adapt to the head curvature. Specifically, each level is made of custom mixtures of urethane rubber and graphite powder adjusted to reach a good trade-off between high permittivity and low losses, as indicated in Table 1, which reports the proportions of used materials and their resulted dielectric properties at 1 GHz, respectively. From back to front, the first layer, dubbed G35, acts as the support substrate of the antenna. While the second one, G25, is a matching medium that minimizes the antenna-to-head mismatch.
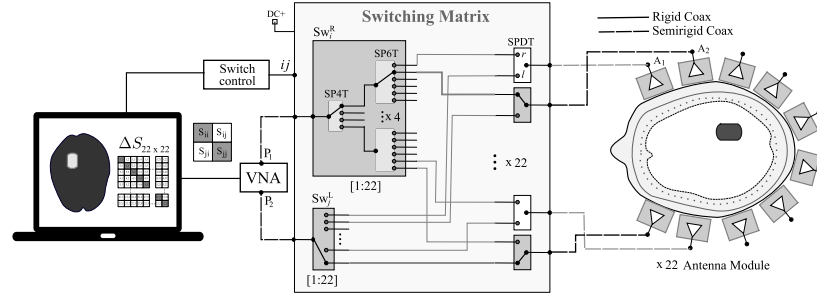
(a)

(b)

Fig. 2: Microwave brain imaging system prototype. (a) Scheme. (b) Photo: (A) Laptop, (B) vector network analyzer, (C) switch interface card, (D) DC power source, (E) switch control card, (F) switching matrix, (G) head phantom with antenna array on top.

Table 1: Antenna mixtures composition and their permittivity at 1 GHz

	Graphite [%]	Rubber [%]	ϵ_r	σ [S/m]
Matching	25	75	13	0.18
Substrate	35	65	18	0.3

The optimized antenna works in a -10 dB band from 0.85 to 1.25 GHz in the head vicinity, with transmission parameters between antenna pairs between -80 to -40 dB (see Fig. 3(b)). The antennas reach adequate EM wave penetration at 1 GHz into the head with either homogeneous and multi-tissue head models, as shown in Fig. 4, and cover the upper head domain if we consider a conformal 22-antenna array placed all around the head (see Fig. 2). For penetration analysis, we estimate
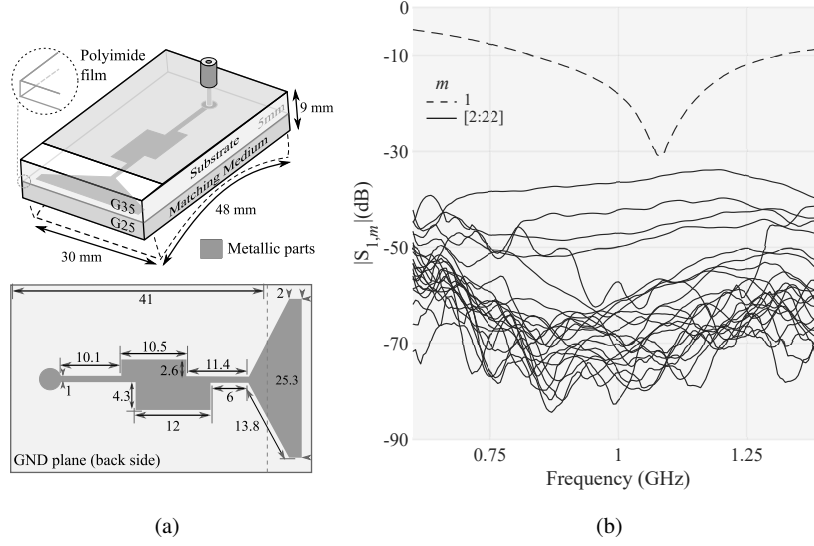
Fig. 3: Flexible custom-made antenna module and measured S-parameters amplitude. (a): antenna diagram with all dimensions in mm (see the manufactured antenna in Fig. 5(c-d)). (b): S-parameters for one antenna of the MWI system.

the power density, $\mathbf{W}_{av}$, associated with the time average Poynting vector (average power density) as [32]:

$$\mathbf{W}_{av} = \frac{1}{2}[\mathbf{E} \times \mathbf{H}^*], \tag{9}$$

where $\mathbf{E}$ and $\mathbf{H}$, electric and magnetic fields, respectively, are computed via a full-wave simulation with two lateral conformal placed antennas. The details of the head models are discussed in the numerical validation section. Overall, the antenna module combines the benefits of a flexible antenna with the cheap cost, low complexity, and adaptability of a traditional circuit-printed one, and working within a low-complexity array complies with the requirements demanded by the MWI application.

3.2 Vector Network Analyzer

The vector network analyzer (VNA) is an instrument that measures the constituent wave quantities, e.g., a_1, b_1, or the related phase and magnitude of the S-parameters of passive and active devices. Depending on the application, these measures involve one or more ports, over-swept frequency, or power. For example, we use the swept frequency for characterizing the dielectric properties of the used materials in the experimental part and the MWI monitoring test. Thus, the VNA provides input
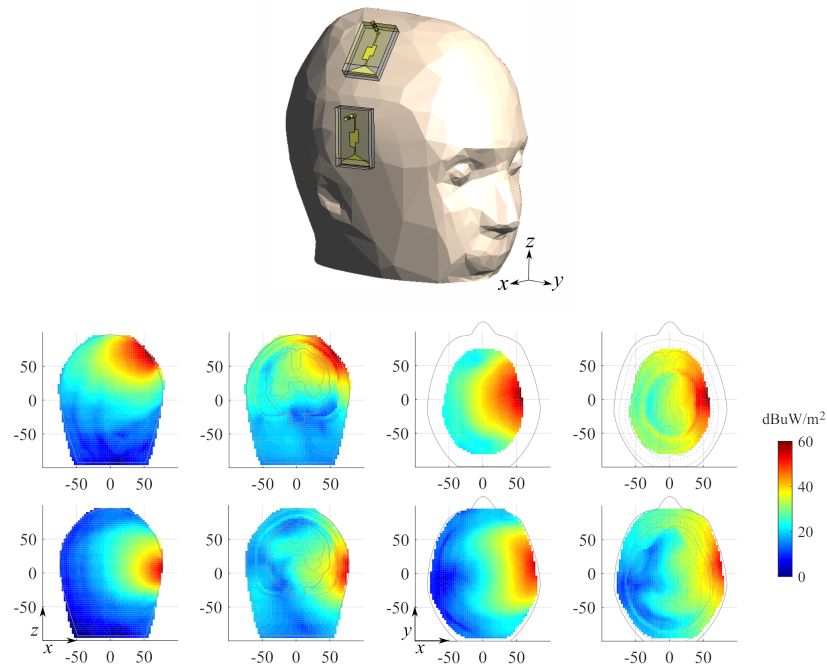
Fig. 4: Sagittal and transverse plane view of the power distribution within the head models for two different lateral antennas. From left-to-right: 1st and 3rd, homogeneous head; 2nd and 4th, multi-tissue head. Top-row:Antenna 1. Bottom-row:Antenna 2. Dimensions in [mm].

signals at the different ports while acquiring incident and reflected waves at each port. So, internally it consists of a signal source generator, some receivers, and some directional devices for separating incident and reflected energy [34].

The VNA is an excellent MWI prototyping instrument. It gives an overall design and testing flexibility, allowing us to gather the needed S-parameter of the imaged situation in multiple configurations and scenarios. Though, its use can be replaced for ad-hoc or customizable devices [35–37]. As the technology's proof-of-concept stage, we opt for the compact Streamline USB Vector Network (P9375A Keysight, 10 MHz–26 GHz) for the presented device in this work [38]. This VNA guarantees gathering the MWI duty information with a noise floor at about -110 dB (at 1 GHz), using an intermediate filter (IF) set at 100 Hz, in a single measure, i.e., without averaging.

3.3 Switching matrix

The switching matrix is the block of the MWI system that allows for measuring the full S-parameter matrix of the 22×22 antenna array using a 2-port VNA in a multistatic multiview configuration. Then, the switching matrix multiplexes each possible antenna pair, sequentially transmitting and receiving, while completing the full matrix by 2×2 segments. Notice, then, that measure of the matrix is not an instantaneous one. However, considering the target application with much slower variation rates and the controlled condition of the experimental testing, it can be considered instantaneous.

The matrix architecture consists of a two-arm one, where each one-to-twenty arm is connected to a VNA port and to twenty-two selecting switches, which set the operating antenna pair as shown in Fig. 2 (a). The arms, SW^R and SW^L in the figure, are implemented using a single-pole-four-throw (SP4T) and four single-single-pole-six-throw (SP6T), while selecting ones with pole-double-throw (SPDT), all electromechanical coaxial ones, with low insertion (<0.3 dB) loss and high isolation (>90 dB) [39]. Here it is worth noticing that although the advantageous isolation given by the electromechanical switches, they have drawbacks such as slow sweep rate, repeatability, typically no better than a few hundredths to a tenth of a dB at microwave frequencies, and limited lifetime [34]. Thus, updating the switches to solid-state ones would substantially improve the time performance and repeatability, as exhibited in [40], rendering the system real-time responsive. Currently, it spends around five minutes by acquisition set, depending on the VNA setup. Moreover, the connections between the internal sections of the matrix are made with semi-rigid coaxial cable, and the external connections with semi-flexible coaxial ones, and a DC source powers the matrix, and a control card using the VISA/TCPIP (VXI-11) protocol on an Ethernet connection handles it.

3.4 Phantoms

In order to validate the prototype in a meaningful scenario, we employ an anthropomorphic head phantom and a realistic non-static stroke one. For the former, the phantom is based on an anthropomorphic 3-D model of an adult head derived by modifying models from [25,41,42] as a single-cavity one, considering just the external layer. Moreover, we attach to it the antenna supports as shown in Fig. 5 (a-b). It is 3-D printed using polyester casting resin, which has dielectric properties similar to plastic ($\epsilon_r \approx 3$) and thickness around 3 mm. So, electromagnetically it may compare with air gap with the same thickness, as studied in [26]. For the latter, we develop a non-static phantom (custom balloon) that mimics the spatial evolution of an early-onset situation, i.e., it can evolve during the monitoring, allowing us to assess the system's capabilities for tracking the change. The phantom shape is abstracted by segmenting CT medical images[1], and 3-D printed using a PVA 3D filament [43], with the printer's minimum thickness extrusion setting (around 0.1 mm) and the

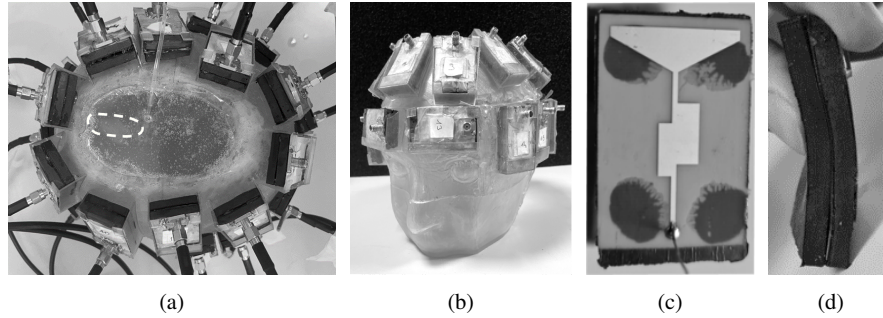(a)   (b)   (c)   (d)

Fig. 5: Manufactured head phantom and antenna array. (a): top view, the dashed contour indicates the position of the stroke. (b): isometric view. (c): radiant part of the antenna – top view. (d): lateral view of the antenna.

number of layers by thickness set to one as can be seen in Fig. 6(a), to reduce the mold material. Then, the printed stroke model, Fig. 5(b-c), is coated using a thin layer (less than 1 mm) of slow-cure platinum silicone layer [44], letting cured it as shown in Fig. 5 (d). The last step exploits the water-soluble nature of the PVA, dissolving the mold by injecting water and then removing the residuals via a small hole, which is used later to attach it to a 3 mm-radius feeding cannula. The result is a resistant, multi-use, and shape-realistic stroke phantom.

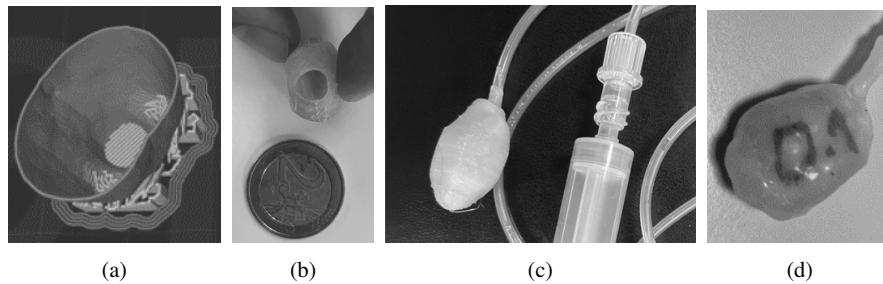(a)   (b)   (c)   (d)

Fig. 6: Stroke phantom manufacturing. (a): 3-D model cut view. (b): PVA mold. (c): Model sealed. (d): Stroke phantom before of remove PVA material.

The phantoms are filled with Triton-X-based mixtures, mimicking the dielectric properties of the head and the stroke, respectively. The recipes for the employed liquid mixtures are based on [41], and are reported in Table 2, together with the corresponding target dielectric parameters (i.e. relative permittivity, ϵ_r, and conductivity, σ [S/m]). In Table 1, HEM and ISC stand for the hemorrhagic, and ischemic stroke cases, which real reference values are taken from [22, 23], and brain refers to the average dielectric properties of the brain tissues considering a compound of 75% of white matter and 25% of grey matter [41].

Table 2: Mimicking Materials Composition and Permittivity at 1 GHz

	Triton X-100 [%]	Water [%]	Salt [%]	ϵ_r	σ [S/m]
ISC	50	50	5.2	34	0.6
HEM	14	86	9.4	68	1.5
Brain	38	62	5.2	45	0.7

The filled head is depicted in Fig. 5(a), where the stroke one is introduced from the top, and signaled by the dashed white contour. Also, Fig. 7 presents the stroke changing in volume from empty to a maximum of 15 cm^3, states used later during the numerical and experimental validation.

(a) Empty   (b) 5 cm^3 (c) 10 cm^3 (d) 15 cm^3
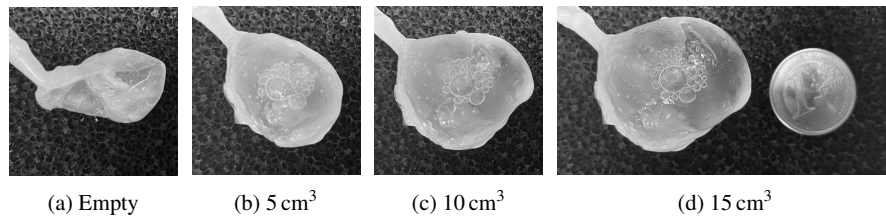
Fig. 7: Non-static stroke phantom growth.

4 Numerical Validation

This section presents a thorough numerical analysis of the projected MWI device, working as an instrument of design and validation in fully controlled conditions. It approaches the assessments using realistic full-wave simulations and the imaging algorithm described in the previous section. The analysis focuses first on the imaging operator's capabilities and then on the monitoring imaging capabilities.

4.1 Imaging Operator

The operator is an essential component of the imaging, $\mathcal{L}$ in Eq. 4, being fundamental to reaching outcomes with adequate accuracy, reliability, and quality. It is the framework of the imaging, in which the input differential scattering matrix is projected, and a non-well-conditioned operator might degrade the retrieved images, even in an ideal noiseless condition. Thus, the operator should include a complete

[1] Work in collaboration with the Emergency Medicine Dept. of Lariboisière University Hospital, Ilumens Health Simulation Center and Sorbonne University, all in Paris (FR).

and faithful description of the MWI system. With the previous premise in mind, we built the operator of our system using full-wave simulations, including a detailed and highly realistic description of all antennas and their respective layout on top of the head. Though the description of the head is approached using a simplified single-tissue head model (ϵ_r = 45, and σ = 0.7 [S/m] at 1 GHz), considering that it changes from patient to patient in a real clinical scenario, and the exact morphology of head under test is unknown.

Once built the operator, we analyze it using its decomposed version (see Eq. 5), which is described by Fig. 8. Though, finer details correspond to singular values which are lower in magnitude, whose contribution to the data is most likely overwhelmed by measurement noise and model errors. Therefore, considering the actual dynamic range available for the differential signal is around 30 dB, we select an operator truncation (T in Eq. 5) which keeps approximately the first 180 singular values, corresponding to values of not lower than 30 dB with respect to the highest one, σ_1,
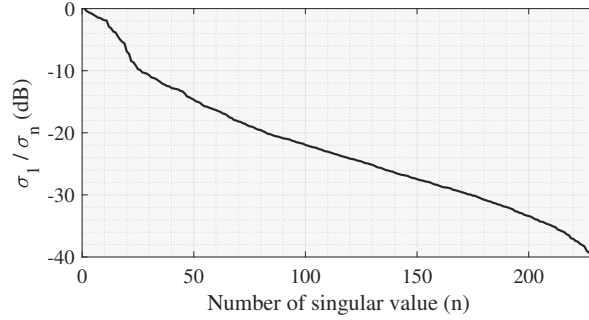

Fig. 8: Imaging kernel singular value behavior.

Moreover, to assess the effect of the truncation on spatial resolution, we evaluate the PSF as:

$$[\Pi_{n_T}] = \sum_{n=1}^{n_T} [v_n]\langle\,\cdot\,, [v_n]\rangle, \tag{10}$$

for both the full and truncated operator. It represents the orthogonal projection of the contrast functions spanned by the first, n_T, of right singular vectors, $[v_n]$, of $\mathcal{L}$, onto the finite-dimensional space [30]. So, it indicates the contrast that can be retrieved using a specific n_T. In the specific, we use Eq. 10 considering an ideal point-like contrast, i.e., setting $\Delta\chi$ = 1 in a 3 mm voxel, while $\Delta\chi$ = 0 for all the others elements of DOI.

Finally, Fig. 9 presents the normalized retrieved images, where a minimal variation between cases can be noticed. It confirms that the selected truncation has negligible worsening effects on the system resolution. Then, defining the resolution as the points at -3 dB of the normalized projection, the system shows a centimetric resolution,

being around $\lambda/4$, in agreement with [30]. However, the resolution is not symmetrical on all axis, having the major resolution loss along the vertical axis (z-axis), which is reasonable considering the antenna array distribution.
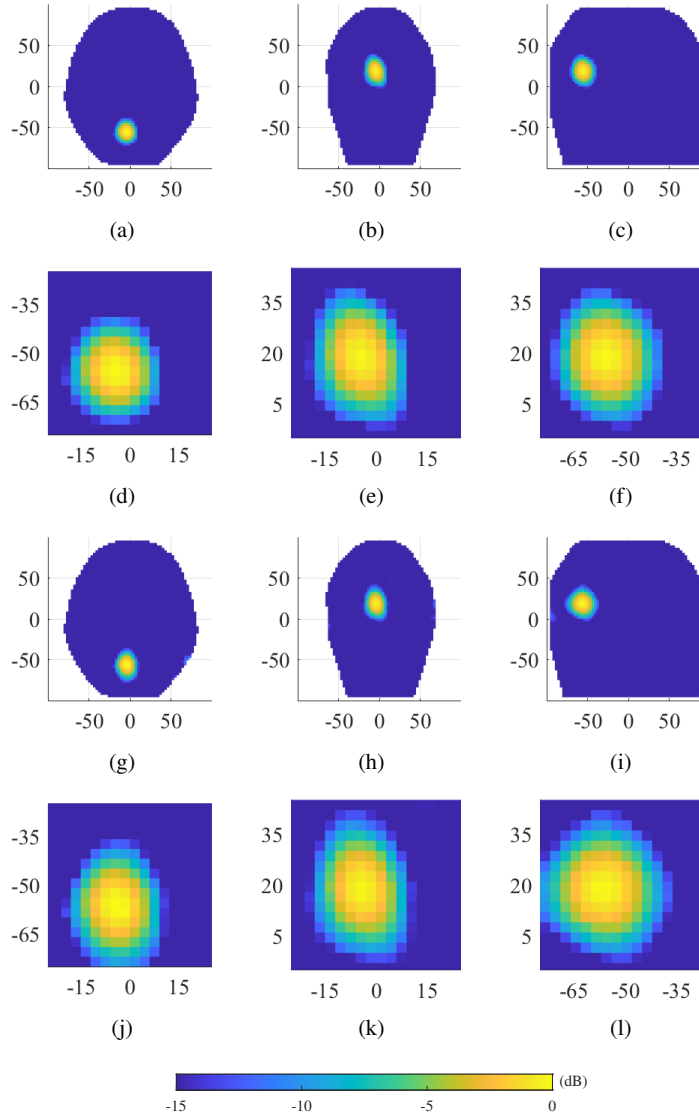

Fig. 9: Normalized projection of 3 mm voxel in the imaging operator. (a-f): Imaging using the full operator. (g-l): Imaging truncating the operator at -30 dB. Dimensions in mm.

4.2 Numerical Brain Stroke Monitoring

In this second stage of numerical validation, we evaluate the imaging capabilities of the system testing in monitoring scenarios of early-stage stroke onset. The stroke is placed between the occipital and parietal zones of the brain (posterior head), miming an actual medical condition that affects the visual functions [45]. Regarding the stroke dimensions, it is projected as temporal dynamic spatial evolution changing its volume from 5 to 15 ċm^3, which is represented in Fig. 10, while considering either hemorrhagic and ischemic typologies of stroke. Moreover, we evaluate each condition using an average single-tissue head model and a multi-tissue one, where each tissue is homogeneous and takes the electric properties shown in the table in Fig. 10 [21]. For the sake of visualization, Fig. 10 reports the skin as the head contour, though, in the simulated model, it has a thickness of around 3 mm. Also, it is worth highlighting that the operator in all following tests, even the experimental ones, is computed using the homogeneous head model.
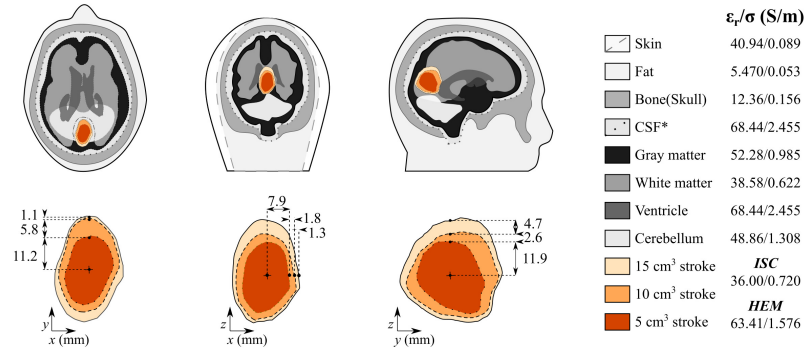

Fig. 10: Numeric mimicked stroke condition considering a multi-tissue head model, and 5, 10 and 15 cm^3 volumetric variations. From left-to-right: transverse, coronal and sagittal plane views cut at the center of the ill-affected area. *CSF stands for cerebro spinal fluid. ϵ_r and σ at 1 GHz.

The simulated virtual scenarios provide the scattering matrix, s, changing the stroke volume by 5 ċm^3, at each state. Hence, three temporal differential scattering matrices, $\Delta S = S(t_0) - S(t_s)$, are considered. These represent changes from the healthy or without of the stroke to $s = 1$ to 5 cm^3 stroke volume, $s = 2$ to 10 cm^3, and $s = 3$ to 15 cm^3, respectively. Notice, also, that due to the anthropomorphic shape of the stroke, the radial variations from the center of the stroke are not linear between states, as shown in Fig. 10 (bottom row). They depend on the state change and span between 1 to 12 mm in the main axis.

4.2.1 Homogeneous case

(a) $5\,\mathrm{cm}^3$ (b) $10\,\mathrm{cm}^3$ (c) $15\,\mathrm{cm}^3$
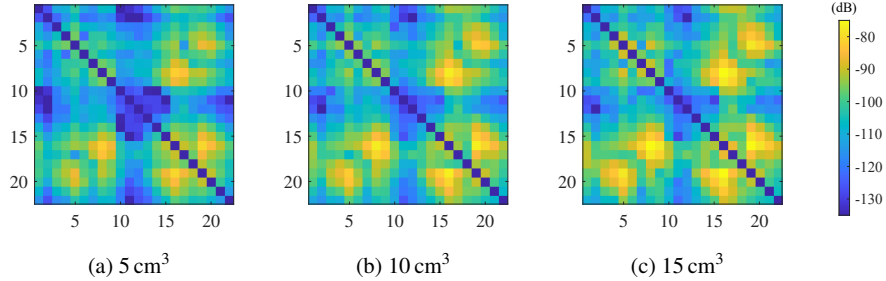
Fig. 11: Simulated differential S-parameters for the different hemorrhagic cases using the homogeneous head. The axis indicate the antenna index.

Firstly, we report the differential scattering matrix, $\Delta S_{22\times 22}$, at 1 GHz for the three named situations in Fig. 11. From these, we null the reflection coefficients (diagonal) mimicking the experimental approach, where these demonstrate a sensibility to the manufacturing tolerance of the antenna that is not numerically considered, introducing a modeling error that harms the imaging. Moreover, notice that the matrices show a non-forced symmetry between the top and bottom triangular matrix, as expected from the transmission coefficients. Thus, the reconstruction algorithm employs either one of the triangular matrices for the imaging. Also, regarding the specific studied cases, it can be glance the matrices presents a high similarity, mainly changing the intensity of certain areas in all three cases. This is expected since they share a common baseline, and the variation is concentrated in a relatively small area.

Applying the imaging algorithm, with the truncation index set at -30 dB, we obtain 3-D electrical contrast maps of the hemorrhagic situation, reporting them in Fig. 12. It depicts the normalized amplitude using a zoomed-up and regular visualization of 2-D and 3-D representations to see the details and indicate the stroke localization. For the 2-D one, we cut at the center of the ill-affected area and plot the transverse, sagittal, and frontal planes, respectively. Instead, for the 3-D one, we plot the voxel with values below -3 dB. Additionally, we include dotted red contours signaling the actual stroke shape on the plane.

Closing the virtual assessment, we also consider the ischemic condition using the same volume variation and changing the dielectric properties of the stroke-affected area. Thus, as expected, and considering we are reporting qualitative images, i.e., we are not discriminating the stroke typology from the images as in the tomographic approaches, the results of the ischemic case are analogous to the hemorrhagic one as shown in Fig. 13, where 0-15 cm^3 scenario is presented. The non-reported cases, compared to the hemorrhagic results, show similar agreement.
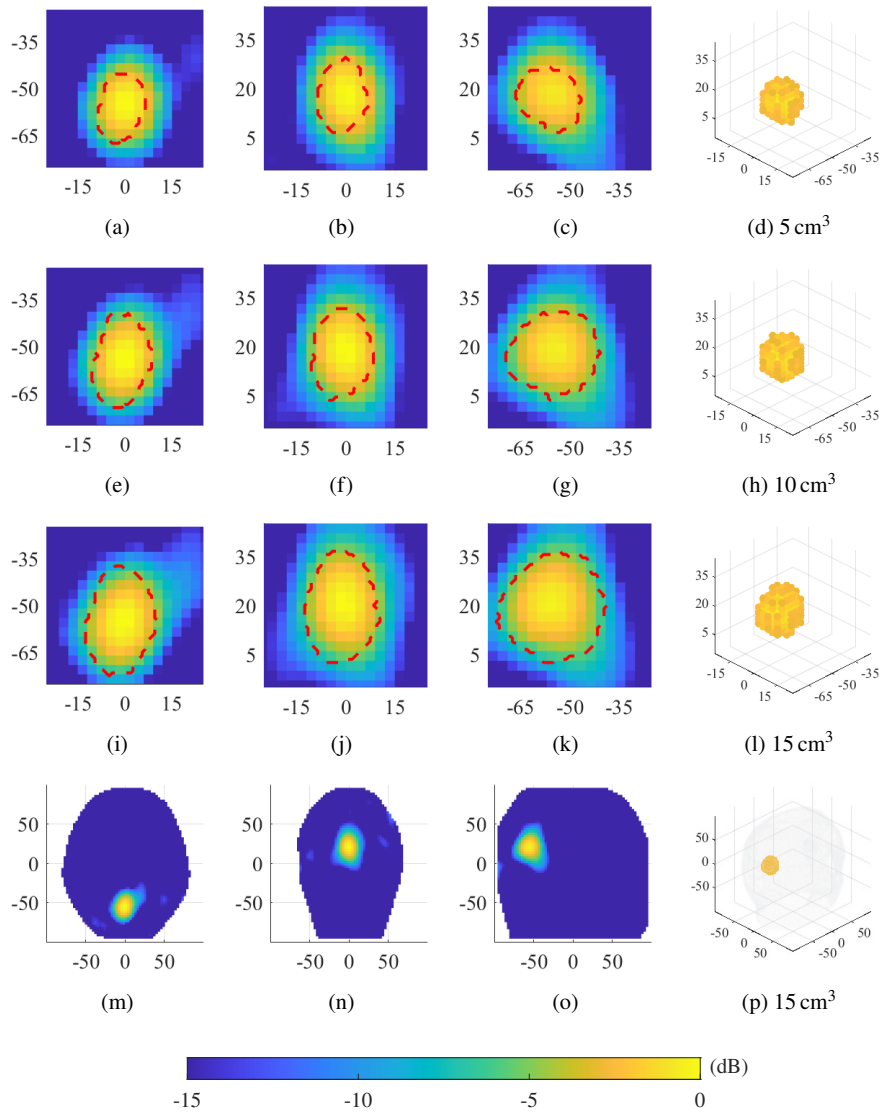
Fig. 12: Normalized amplitude values of the retrieved dielectric contrast for the different hemorrhagic cases using the homogeneous head. (a-d) 0-5 cm^3; (e-h) 0-10 cm^3; (i-p) 0-15 cm^3. The 3-D views indicate the values above -3 dB.
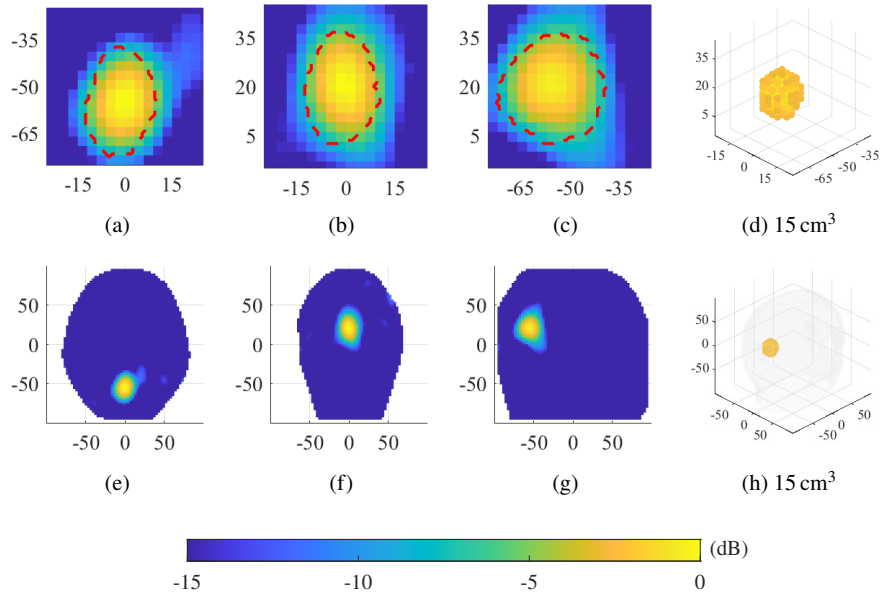
Fig. 13: Normalized amplitude values of the retrieved dielectric contrast for the 0-15 cm^3 ischemic case using the homogeneous head. The 3-D views indicate the values above -3 dB.

4.2.2 Multi-tissue case

Here we evaluate the algorithm's capabilities to perform in a more realistic clinical scenario, considering first a more complex model of the head and second, the unknown specific morphology of each patient. Hence, we use a homogeneous-head-based operator for the imaging while obtaining the differential scattering parameters using a multi-tissue head model. The pathological evolution of the stroke status, i.e., the three-volume state variation and both typologies, are considered as it was in the homogeneous analysis.

Following the same results scheme, first, we present the differential scattering for the three case variations of a hemorrhagic stroke in Fig. 14. As in the homogeneous case, the matrices present evident resemblances due to the common elements differing in the intensity of some specific areas. Interestingly, the pattern similarity of the multi-tissue scenarios matrices also extends to the homogeneous ones, indicating the effect of the contrast variation of those.

Starting with the hemorrhagic case, the figure presents normalized reconstructions for all three studied scenarios. In this case, the overall retrieved contrasts show good stroke localization and volume track capability, which is very promising. However, the shape estimation deteriorated significantly on the y-axis, as seen from the sagittal

(a) $5 \, cm^3$ (b) $10 \, cm^3$ (c) $15 \, cm^3$
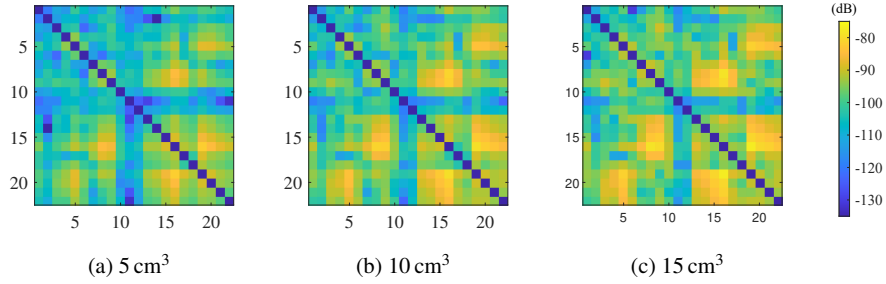
Fig. 14: Simulated differential S-parameters for the different hemorrhagic cases using the multi-tissue head. The axis indicate the antenna index.

plane views. Besides, the results present artifacts, nonexistent in the homogeneous case.

As in the homogeneous case, the ischemic results demonstrate similar outcomes, showing the same positive aspects and identical drawbacks, as expected. Figure 16 depicts the case for $15 \, cm^3$.

In general, the obtained outcomes of all studied cases demonstrate the capabilities to detect, localize and monitor the spatial evolution of the stroke. When the operator describes the situation closely, i.e., the homogeneous case, there is a clear and accurate reproduction, with almost no artifacts. However, the system presents limitations in the most complex and realistic situations, resulting in quality-decreased results due to the distortion of the imaging operator. It is an intrinsic limitation that must be approached before moving to a clinical scenario, though the capabilities to perform precise detection and localization and, to some extent, trace the change of the stroke-affected area is precious medical information.

5 Experimental Validation

The last part of the system validation relies on an experiment mimicking a worsening hemorrhagic condition using the prototype and the phantoms described in Sec. 3. The non-static stroke phantom is positioned in the head, entering from the top, and filled via a cannula and a syringe. With this procedure, we set, one at a time, the different studied states of the stroke, i.e., empty stroke (healthy), $5 \, cm^3$, $10 \, cm^3$, and $15 \, cm^3$, while measuring the scattering parameters. Here, we set the VNA input power to -5 dBm, and the intermediate filter (IF) to 100 Hz, reaching a noise floor around -100 dB at 1 GHz.

Figure 17 shows the differential measured scattering matrices, omitting the reflection terms due to their high dependence on the antenna's manufacturing variability, which is hard to include in the numerical model. However, the transmission parameters respond similarly to what expected from the numerical analysis, having
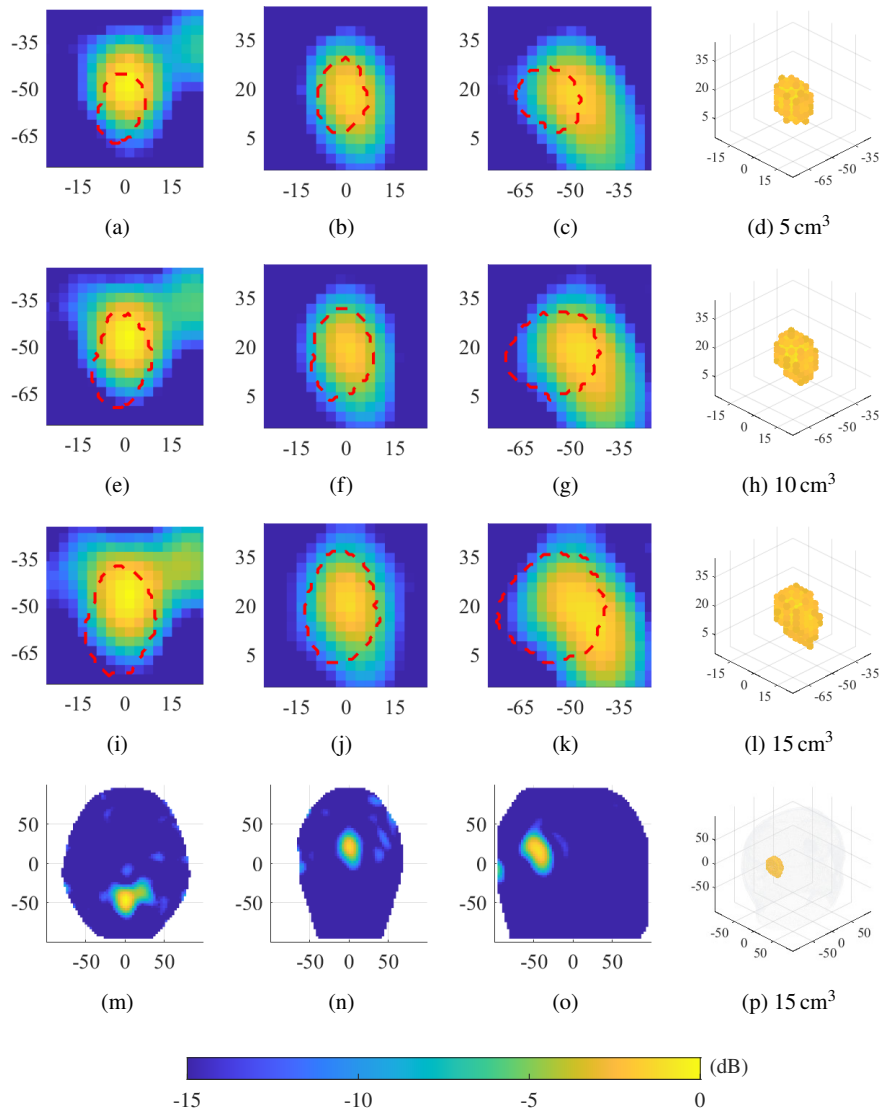
Fig. 15: Normalized amplitude values of the retrieved dielectric contrast for the different hemorrhagic cases using the multi-tissue head. (a-d) 0-5 cm^3; (e-h) 0-10 cm^3; (i-p) 0-15 cm^3. The 3-D views indicate the values above -3 dB.
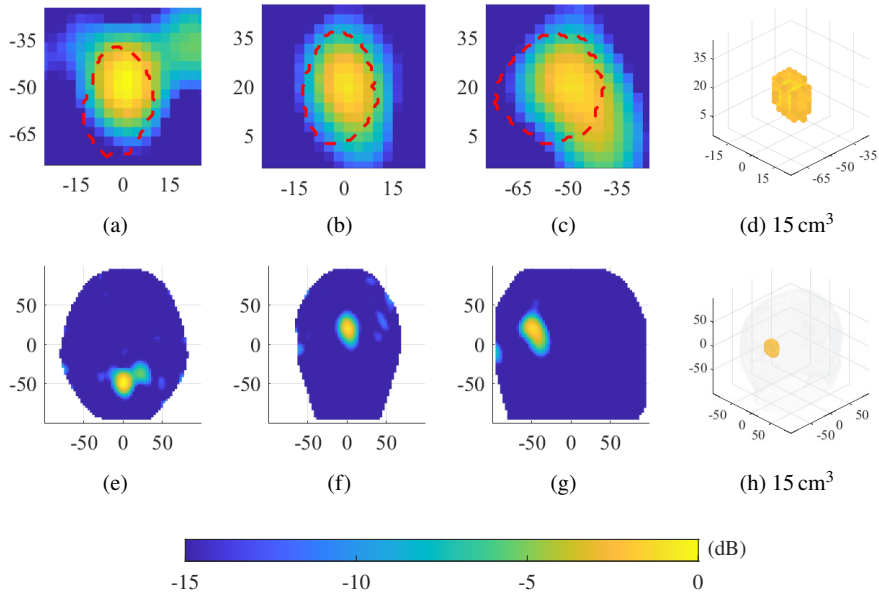
Fig. 16: Normalized amplitude values of the retrieved dielectric contrast for the 0-15 cm^3 ischemic case using the multi-tissue head. The 3-D views indicate the values above -3 dB.

consistent response patterns but with different intensities depending on the considered case. Moreover, as compared to numerical simulations they present lower intensity values, possibly caused by non-modeled sources of loss. Nevertheless, this is adjustable with calibration if required [12, 24]. Also, the matrices exhibit a the mild asymmetry caused by the slight differences in the left and right paths of the switching matrix (see Fig. 2).

Moving to the imaging, we opt for using a truncation index set as -25 dB, retrieving the normalized contrast summarized in Fig. 18, where the main plane views are cut at their maximum value. Moreover, three dotted red circles with radii 10.6, 13.7 and 15.3 mm, corresponding to spheres of volume 5 ,10, and 15 cm^3, act as a visual reference. In agreement with the numerical results, the experiment demonstrates the system's capability to detect and localize the stroke in all cases and estimate and indicate the volume change with a centimetric resolution. Regarding the shape retrieval, it was difficult to determine it with certainty using the tested experimental setup, thus being a point to improve in future testing.

Additionally, we perform both repeatability and false-positive tests as further validation, considering the experimental nature of the data, summarized in Fig. 19. For the repeatability test, we retrieve the 0-5 cm^3 case twice using different measurement sets, achieving equivalent outcomes as shown in Fig. 19 (a - b). For the false-positive

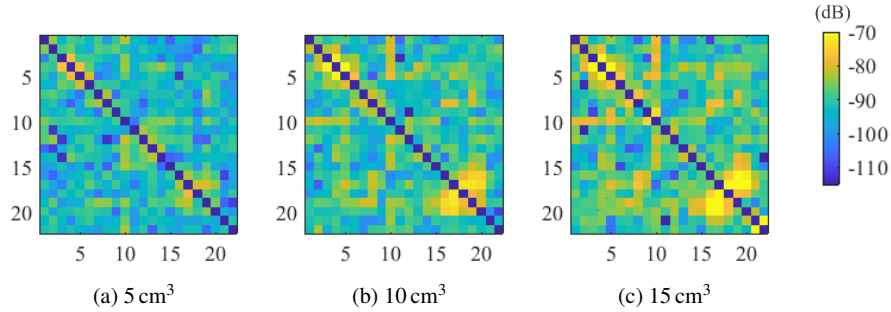(a) 5 cm^3 (b) 10 cm^3 (c) 15 cm^3

Fig. 17: Measured differential S-parameters for the different hemorrhagic cases using the homogeneous head. The axis indicate the antenna index.

test, the differential matrix is made by subtracting the parameters of two empty cases and normalizing the contrast with the maximum of the previous cases as a reference. As shown in Fig. 19 (c), the device can discriminate this condition as well.

6 Conclusion and Perspectives

In this chapter, we have presented the design, implementation and validation of a low-complexity microwave-based scanner for brain stroke imaging. The prototype comprises a 22-element array of custom-designed flexible antennas working around 1 GHz, with a differential retrieval algorithm that allows almost real-time imaging. The system is tested in realistic mimicked scenarios, demonstrating its capabilities to detect, localize and trace temporal-spatial variations of both hemorrhagia and ischemia with a centimetric resolution. It also shows the potential to operate even in the absence of morphological patient information.

Future work aims to extend the system's validation in other relevant conditions, including tests with experimental multi-tissue phantoms and imaging operators with additional a-priori information, for example, multi-frequency ones, or, operators based on mimicked heads with two or three homogeneous zones. Moreover, it is expected to upgrade the hardware components with ad-hoc devices that replace the VNA and the switching, improving the overall measuring-time performance, a bottle-neck of the device.
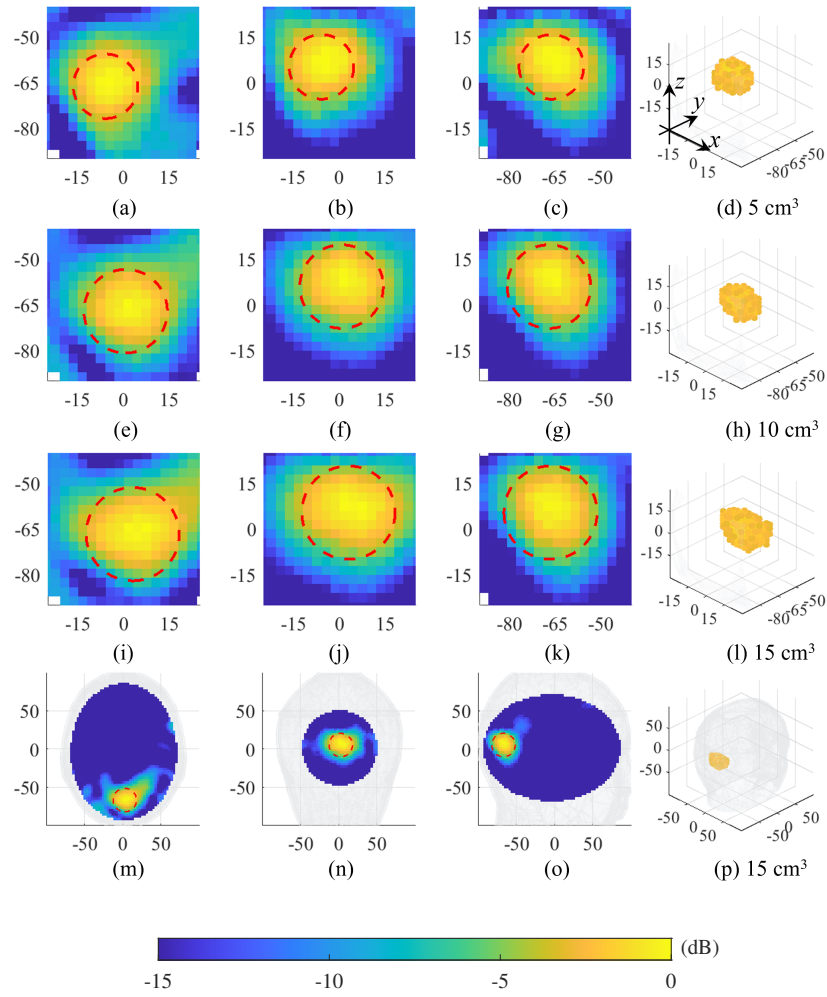
Fig. 18: Experimental test: normalized amplitude values of the retrieved dielectric contrast for the different hemorrhagic cases using the homogeneous head. (a-d) 0-5 cm^3; (e-h) 0-10 cm^3; (i-p) 0-15 cm^3. The 3-D views indicate the values above -3 dB.
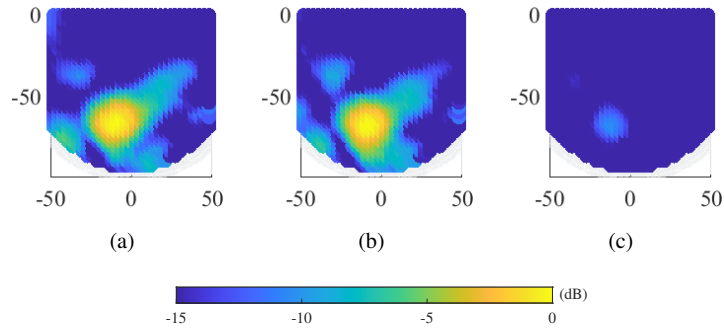
Fig. 19: Transverse views center at the maximum, amplitude normalized of the reconstructed dielectric contrast. (a - b) repeatability, two 0-5 cm^3 cases using a different set of measurements. (c) false-positive test, difference between two empty cases normalized at maximum value of (a).

References

1. Robert Felberg and Andrew Naidech. The five ps of acute ischemic stroke treatment: Parenchyma, pipes, perfusion, penumbra, and prevention of complications. *The Ochsner journal*, 5:5–11, 12 2003.

2. Kyle B Walsh. Non-invasive sensor technology for prehospital stroke diagnosis: Current status and future directions. *International Journal of Stroke*, 14(6):592–602, 2019. PMID: 31354081.

3. Na Hu, Tianwei Zhang, Yifan Wu, Biqiu Tang, Minlong Li, Bin Song, Qiyong Gong, Min Wu, Shi Gu, and Su Lui. Detecting brain lesions in suspected acute ischemic stroke with ct-based synthetic mri using generative adversarial networks. *Annals of translational medicine*, 10(2):35, 2022.

4. Igor Bisio, Alessandro Fedeli, Chiara Garibotto, Fabio Lavagetto, Matteo Pastorino, and Andrea Randazzo. Two ways for early detection of a stroke through a wearable smart helmet: Signal processing vs. electromagnetism. *IEEE Wireless Communications*, 28(3):22–27, 2021.

5. Alessandro Fedeli, Valentina Schenone, Andrea Randazzo, Matteo Pastorino, Tommy Henriksson, and Serguei Semenov. Nonlinear s-parameters inversion for stroke imaging. *IEEE Transactions on Microwave Theory and Techniques*, 69(3):1760–1771, 2021.

6. Pan Lu and Panagiotis Kosmas. Three-dimensional microwave head imaging with gpu-based fdtd and the dbim method. *Sensors*, 22(7), 2022.

7. Olympia Karadima, Pan Lu, Ioannis Sotiriou, and Panagiotis Kosmas. Experimental validation of the dbim-twist algorithm for brain stroke detection and differentiation using a multi-layered anatomically complex head phantom. *IEEE Open Journal of Antennas and Propagation*, 3:274–286, 2022.

8. Ondrej Fiser, Vojtech Hruby, Jan Vrba, Tomas Drizdal, Jan Tesarik, Jan Vrba, and David Vrba. Uwb bowtie antenna for medical microwave imaging applications. *IEEE Transactions on Antennas and Propagation*, pages 1–1, 2022.

9. Abdulrahman S. M. Alqadami, Adnan Trakic, Anthony E. Stancombe, Beadaa Mohammed, Konstanty Bialkowski, and Amin Abbosh. Flexible electromagnetic cap for head imaging. *IEEE Transactions on Biomedical Circuits and Systems*, 14(5):1097–1107, 2020.

10. Abdulrahman S. M. Alqadami, Ali Zamani, Adnan Trakic, and Amin Abbosh. Flexible electromagnetic cap for three-dimensional electromagnetic head imaging. *IEEE Transactions on Biomedical Engineering*, 68(9):2880–2891, 2021.

11. Jorge A. Tobon Vasquez, Rosa Scapaticci, Giovanna Turvani, Gennaro Bellizzi, David O. Rodriguez-Duarte, Nadine Joachimowicz, Bernard Duchêne, Enrico Tedeschi, Mario R. Casu, Lorenzo Crocco, and Francesca Vipiana. A prototype microwave system for 3d brain stroke imaging. *Sensors*, 20(9), 2020.
12. David O. Rodriguez-Duarte, Cristina Origlia, Jorge A. Tobón Vasquez, Rosa Scapaticci, Lorenzo Crocco, and Francesca Vipiana. Experimental assessment of real-time brain stroke monitoring via a microwave imaging scanner. *IEEE Open Journal of Antennas and Propagation*, 3:824–835, 2022.
13. Stefan Candefjord, Johan Winges, A. A. Malik, Yinan Yu, Thomas Rylander, Tomas McKelvey, Andreas Fhager, Mikael Elam, and Mikael Persson. Microwave technology for detecting traumatic intracranial bleedings: tests on phantom of subdural hematoma and numerical simulations. *Medical & Biological Engineering & Computing*, 55:1177 – 1188, 2016.
14. Mikael Persson, Andreas Fhager, Hana Dobiek Trefna, Yinan Yu, Tomas McKelvey, Göran Pegenius, Jan-Erik Karlsson, and Mikael Elam. Microwave-based stroke diagnosis making global prehospital thrombolytic treatment possible. *IEEE Transactions on Biomedical Engineering*, 61:2806–2817, 2014.
15. Serguei Semenov, Markus Hopfer, Ramon Planas, Abouzar Hamidipour, and Tommy Henriksson. Electromagnetic tomography for brain imaging: 3d reconstruction of stroke in a human head phantom. In *2016 IEEE Conference on Antenna Measurements Applications (CAMA)*, pages 1–4, 2016.
16. David Cook, Helen Brown, Isuravi Widanapathirana, Darshan Shah, James Walsham, Adnan Trakic, Guohun Zhu, Ali Zamani, Lei Guo, Aida Brankovic, Ahmed Al-Saffar, Anthony Stancombe, Alina Bialkowski, Phong Nguyen, Konstanty Bialkowski, Stuart Crozier, and Amin Abbosh. Case report: Preliminary images from an electromagnetic portable brain scanner for diagnosis and monitoring of acute stroke. *Frontiers in Neurology*, 12, 2021.
17. M. Bertero and P. Boccacci. *Introduction to Inverse Problems in Imaging*. Inst. Phys., Bristol, U.K., 1998.
18. Natalia K. Nikolova. *Introduction to Microwave Imaging*. EuMA High Frequency Technologies Series. Cambridge University Press, 2017.
19. Chen Xudong. *Computational Methods for Electromagnetic Inverse Scattering*. Wiley-IEEE Press, 2018.
20. Valeria Mariano, Jorge A. Tobon Vasquez, and Francesca Vipiana. A novel discretization procedure in the csi-fem algorithm for brain stroke microwave imaging. *Sensors*, 23(1), 2023.
21. D.Andreuccetti, R.Fossi, and C.Petrucci. An internet resource for the calculation of the dielectric properties of body tissues in the frequency range 10 hz - 100 ghz. ifac-cnr, florence (italy), 1997. based on data published by c.gabriel et al. in 1996.
22. David Ireland and Marek Bialkowski. Feasibility study on microwave stroke detection using a realistic phantom and the fdtd method. In *2010 Asia-Pacific Microwave Conference*, pages 1360–1363, 2010.
23. Serguei Y. Semenov and Douglas R. Corfield. Microwave tomography for brain imaging: Feasibility assessment for stroke detection. *International Journal of Antennas and Propagation*, 2008:1–8, 2008.
24. David O. Rodriguez-Duarte, Jorge A. Tobon Vasquez, Rosa Scapaticci, Giovanna Turvani, Marta Cavagnaro, Mario R. Casu, Lorenzo Crocco, and Francesca Vipiana. Experimental validation of a microwave system for brain stroke 3-d imaging. *Diagnostics*, 11(7), 2021.
25. Sergey N. Makarov, Gregory M. Noetscher, Janakinadh Yanamadala, Matthew W. Piazza, Sara Louie, Alexander Prokop, Ara Nazarian, and Aapo Nummenmaa. Virtual human models for electromagnetic studies and their applications. *IEEE Reviews in Biomedical Engineering*, 10:95–121, 2017.
26. David O. Rodriguez-Duarte, Jorge A. Tobón Vasquez, Rosa Scapaticci, Lorenzo Crocco, and Francesca Vipiana. Assessing a microwave imaging system for brain stroke monitoring via high fidelity numerical modelling. *IEEE Journal of Electromagnetics, RF and Microwaves in Medicine and Biology*, 5(3):238–245, 2021.
27. Jin Jianming. *The Finite Element Method in Electromagnetic*. Wiley-IEEE Press, second edition, 2002.

28. Elia A. Attardo, Andrea Borsic, Giuseppe Vecchi, and Paul M. Meaney. Whole-system electromagnetic modeling for microwave tomography. *IEEE Antennas and Wireless Propagation Letters*, 11:1618–1621, 2012.

29. R. Scapaticci, M. Bjelogrlic, J. A. Tobon Vasquez, F. Vipiana, M. Mattes, and L. Crocco. *Emerging Electromagnetic Technologies for Brain Diseases Diagnostics, Monitoring and Therapy*, chapter 2. Microwave Technology for Brain Imaging and Monitoring: Physical Foundations, Potential and Limitations, pages 7–35. Springer int. pub., 2018.

30. Rosa Scapaticci, Jorge Tobon, Gennaro Bellizzi, Francesca Vipiana, and Lorenzo Crocco. Design and numerical characterization of a low-complexity microwave device for brain stroke monitoring. *IEEE Transactions on Antennas and Propagation*, 66(12):7328–7338, 2018.

31. R. Scapaticci, L. Di Donato, I. Catapano, and L. Crocco. A feasibility study on Microwave Imaging for brain stroke monitoring. *Prog. Electromagn. Res. B*, 40:305–324, 2012.

32. C.A. Balanis. *Advanced Enginnering Electromagnetics*. Willeys, 1989.

33. O. M. Bucci, L. Crocco, R. Scapaticci, and G. Bellizzi. On the design of phased arrays for medical applications. *Proc. IEEE*, 104(3):633–648, Mar. 2016.

34. Mohamed Sayed and Jon Martens. *Vector network analyzers*, page 98–129. The Cambridge RF and Microwave Engineering Series. Cambridge University Press, 2013.

35. Mario R. Casu, Marco Vacca, Jorge A. Tobon, Azzurra Pulimeno, Imran Sarwar, Raffaele Solimene, and Francesca Vipiana. A cots-based microwave imaging system for breast-cancer detection. *IEEE Transactions on Biomedical Circuits and Systems*, 11(4):804–814, 2017.

36. Anthony Edgar Stancombe, Konstanty S. Bialkowski, and Amin M. Abbosh. Portable microwave head imaging system using software-defined radio and switching network. *IEEE Journal of Electromagnetics, RF and Microwaves in Medicine and Biology*, 3(4):284–291, 2019.

37. K. D. Paulsen P. M. Meaney. Theoretical premises and contemporary optimizations of microwave tomography. In K. H. Yeap A. Kishk, editor, *Microwave Technologies*, pages 1–24. IntechOpen, London, 2022.

38. Keysight Technologies. Keysight 2-port and 4-port PNA network analyzer, N5227A 10 MHz to 67 GHz. *Data Sheet and Technical Specifications*, Apr. 2019.

39. Jorge A. Tobon Vasquez, R. Scapaticci, G. Turvani, G. Bellizzi, N. Joachimowicz, B. Duchêne, E. Tedeschi, M. R. Casu, L. Crocco, and F. Vipiana. Design and experimental assessment of a 2D microwave imaging system for brain stroke monitoring. *Int. J. Antennas Propag.*, (Article ID 8065036):12 pages, 2019.

40. Marco Ricci, Bernardita Štitić, Luca Urbinati, Giuseppe Di Guglielmo, Jorge A. Tobón Vasquez, Luca P. Carloni, Francesca Vipiana, and Mario R. Casu. Machine-learning-based microwave sensing: A case study for the food industry. *IEEE Journal on Emerging and Selected Topics in Circuits and Systems*, 11(3):503–514, 2021.

41. Nadine Joachimowicz, Bernard Duchêne, Christophe Conessa, and Olivier Meyer. Anthropomorphic breast and head phantoms for microwave imaging. *Diagnostics*, 85(8):1–12, Dec. 2018.

42. Download visible human project data. Available at https://www.nlm.nih.gov/databases/download/vhp.html.

43. Esun. Available at https://www.esun3d.net/Products/PVA.

44. Smooth-on. Available at https://www.smooth-on.com/product-line/dragon-skin/.

45. Elizabeth L Saionz, Duje Tadin, Michael D Melnick, and Krystel R Huxlin. Functional preservation and enhanced capacity for visual restoration in subacute occipital stroke. *Brain*, 143(6):1857–1872, 05 2020.